THE JOURNAL OF PHYSICAL CHEMISTRY C

Article

Cite This: J. Phys. Chem. C 2019, 123, 22842−22850

pubs.acs.org/JPCC

Electron−Phonon Relaxation at Au/Ti Interfaces Is Robust to Alloying: Ab Initio Nonadiabatic Molecular Dynamics

Yi-Siang Wang,[†] Xin Zhou,[‡] John A. Tomko,[§] Ashutosh Giri,[∥] Patrick E. Hopkins,[§,∥,⊥] and Oleg V. Prezhdo*[,†,#]

[†]Department of Chemistry, University of Southern California, Los Angeles, California 90089, United States

[‡]College of Environment and Chemical Engineering, Dalian University, Dalian, 116622, P. R. China

[§]Department of Materials Science and Engineering, University of Virginia, Charlottesville, Virginia 22903, United States

[∥]Department of Mechanical and Aerospace Engineering, University of Virginia, Charlottesville, Virginia 22903, United States

[⊥]Department of Physics, University of Virginia, Charlottesville, Virginia 22903, United States

[#]Department of Physics and Astronomy, University of Southern California, Los Angeles, California 90089, United States

ABSTRACT: Charge and energy transfer at nanoscale metal/metal and metal/semiconductor interfaces are essential for modern electronics, catalysis, photovoltaics, and other applications. Experiments show that a thin Ti adhesion layer deposited between an Au film and a semiconductor substrate greatly accelerates electron-vibrational energy transfer. We employ ab initio real-time time-dependent density functional theory and nonadiabatic molecular dynamics to rationalize this effect and to demonstrate that it is robust to details of Au−Ti atom alloying at the interface. Both perfect Ti adhesion layers and Ti layers alloyed with Au accelerate the rate of energy transfer by about the same amount. The effect arises because lighter Ti atoms introduce higher frequency vibrations and because Ti atoms exhibit high density of states near the Fermi level of Au. The effect vanishes only when Ti is embedded into Au in the form of isolated atoms, because electronic states of isolated Ti atoms do not cover a sufficiently wide energy range. The calculations demonstrate how one can design novel and robust structures to control and manipulate ultrafast energy transfer in nanoscale devices. The design principles established in the current work can be used to improve heat dissipation and to tailor highly nonequilibrium charge distributions.

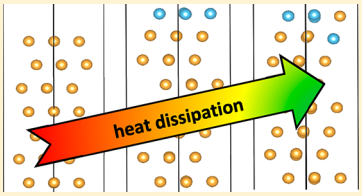

1. INTRODUCTION

Development of electronics, plasmonics and other modern technologies, stimulates extensive experimental and theoretical research on noble metals.[1−13] Continuous size reduction and increased device power densities give rise to extremely large thermal fluxes that inhibit sufficient power dissipation away from heat generation regions, causing self-heating, increasing operation temperatures, and degrading device performance.[14−19] In order to address the heat dissipation problem, one needs to establish relaxation and scattering mechanisms of the fundamental energy carriers in solids. Electron−phonon scattering in particular constitutes a key factor in energy transfer processes that can control a materials' superconductivity, electrical and thermal resistivities, and spin caloritronic properties, and therefore has been studied extensively.[16,20−25] Experimentally, the energy transfer processes are most directly observed with time-resolved pump−probe laser techniques,[21,26−29] while theoretically, the two-temperature model (TTM)[30−34] is often used to explain the thermal equilibration process. The TTM is based on Fourier's law relating heat flux to temperature gradient. It defines hot electron T_e and hot phonon T_p temperatures and describes equilibration between hot electrons and phonons by a single energy transfer rate that makes T_e and T_p equal. For instance, the TTM was used to interpret the recent short-pulsed time-domain thermo-reflectance (TDTR) experiments characterizing the evolution of nonequilibrium between electronic and vibrational degrees of freedom.[35]

The electron−phonon coupling constant, G, used in the TTM is usually derived directly from the measurements. It quantifies the volumetric rate of energy transfer between the two subsystems at different temperatures. In 2005, Chen et al. modified the model by introducing the effective electron−phonon coupling constant, G_{eff}, based on the free electron theory.[36] The theory is valid for free electron metals with a relatively constant density of states (DOS), because it assumes that the DOS is constant over the whole electron temperature range. In 2008, Zhigilei and co-workers introduced further modifications to the TTM and used electronic structure calculations to estimate the electron−phonon coupling constant and study temperature dependence of the electron−phonon coupling factor for several metals.[3] In a parallel effort, Majumdar and Reddy derived an analytic expression describing the contribution of electron−phonon coupling in metals to thermal boundary resistance across metal/nonmetal interfaces.[37] Electron−phonon dynamics in Au films is particularly

Received: July 20, 2019
Revised: August 22, 2019
Published: August 23, 2019

DOI: 10.1021/acs.jpcc.9b06914
J. Phys. Chem. C 2019, 123, 22842−22850

interesting, since Au has a simple structure and allows for a variety of substitutional impurities over broad concentration ranges. Thus, Au provides an excellent testing ground for comparison between theory and experiment. Often, thin transition metal layers are inserted between Au films and substrates, in order to improve adhesion. Unexpectedly, Giri et al. demonstrated that a thin Ti adhesion layer between an Au film and a nonmetal substrate can greatly increase the electron−phonon coupling factor and drastically accelerate the energy relaxation rate (by as much as five-folds compared to a bare Au film deposited on a substrate).[38]

As devices become smaller, energy densities and fluxes grow, systems deviate more and more from thermal equilibrium, and the quasi-equilibrium assumptions underlying the TTM are questionable. In small devices under strong perturbations, energy carrier dynamics become very fast and the energy distributions are highly nonuniform. The ultrafast laser measurements probing these regimes motivate time-domain atomistic simulations to mimic such experiments. Our previous study[39] rationalized the observed[38] strong influence of a thin Ti adhesion layer on the electron−phonon relaxation in an Au film. Using ab initio nonadiabatic molecular dynamics (NAMD) we demonstrated that this strong effect arises because Ti has a DOS within the relevant energy range, and being much lighter than Au, Ti introduces high frequency vibrations that accelerate the dynamics. Since realistic metal/metal interfaces are never perfect, and are particularly prone to alloying, for instance in comparison with interfaces involving semiconductors with directional covalent bonds that impose much more stringent formation conditions, it is important to establish how sensitive the Ti adhesion layer effect is to interfacial imperfections. For this purpose, here, we systematically investigate several Au/Ti structures with different extent of alloying between the two materials, to imitate a realistic Ti adhesion. We demonstrate that the Ti adhesion effect is maintained as long as Ti atoms are not isolated and that the effect is independent of alloying details. The following section describes the essential theoretical background of the ab initio NAMD simulations and provides computational details. The third section presents simulation results, and discusses relationships between chemical composition, geometric and electronic structure, vibrational motions, and electron−phonon relaxation dynamics. The key findings are summarized in the conclusions section.

2. SIMULATION METHODOLOGY

The quantum dynamics simulations of the electron−phonon energy relaxation in Au/Ti alloys are performed using the state-of-the-art methodology developed in our group and combining NAMD[40] with time-dependent density functional theory (TDDFT). NAMD allows one to treat complex systems at the atomistic level of detail, while TDDFT provides an efficient description of electronic properties of condensed matter and nanoscale materials. The approach was introduced in reference,[41] and its implementation within the PYXAID package is detailed in references.[42,43] The current simulation uses the fewest switches surface hopping technique (FSSH),[44] which is the most popular NAMD approach. The methodology has been applied successfully to a broad range of semiconducting and metallic nanoscale systems,[42,43,45−57] including metal films.[25,39,58]

2.1. Nonadiabatic Molecular Dynamics. NAMD treats electrons quantum mechanically and nuclei (semi)classically. It involves solving the time-dependent Schrodinger equation for the electrons coupled to the classical Newton equation for nuclei in a surface hopping type algorithm. Specifically, the time-dependent electronic wave function, $\Psi(\mathbf{r},t;\mathbf{R})$, is expanded in the basis of adiabatic wave functions, $\Phi_n(\mathbf{r};\mathbf{R}(t))$, which depend parametrically on the current geometric configuration along the classical nuclear trajectory, $\mathbf{R}(t)$

$$\Psi(\mathbf{r},\ t;\ \boldsymbol{R}) = \sum_n C_n(t)\Phi_n(\mathbf{r};\ \mathbf{R}(t)) \tag{1}$$

The adiabatic basis is used because it is the most commonly available in atomistic electronic structure codes. The equations-of-motion for the expansion coefficients, $C_n(t)$, are obtained by substituting eq 1 into the time-dependent Schrodinger equation

$$ih\frac{\partial}{\partial t}\Psi(\mathbf{r},\ t;\ \mathbf{R}) = H(\mathbf{r},\ t,\ \mathbf{R})\Psi(\mathbf{r},\ t;\ \mathbf{R}) \tag{2}$$

The resulting equation

$$ih\frac{\partial}{\partial t}C_n(t) = \sum_j C_n(t)(\varepsilon_j\delta_{nj} + d_{nj}) \tag{3}$$

contains the energy ε_j of the adiabatic state j, and the nonadiabatic coupling (NAC) d_{nj} between adiabatic states n and j is given by

$$d_{nj} = -ih\frac{\left\langle \Phi_n|\nabla_{\mathbf{R}}H|\Phi_j\right\rangle}{\mathrm{E}_n - \mathrm{E}_j}\cdot\frac{\mathrm{d}\mathbf{R}}{\mathrm{d}t} = -ih\left\langle \Phi_n\middle|\nabla_{\mathbf{R}}\middle|\Phi_j\right\rangle\frac{\mathrm{d}\boldsymbol{R}}{\mathrm{d}t}$$
$$= -ih\left\langle \Phi_n\middle|\frac{\partial}{\partial t}\middle|\Phi_j\right\rangle \tag{4}$$

The NAC arises from the dependence of the adiabatic states on the nuclear coordinates. In the current calculations it is obtained numerically using the rightmost part of eq 4, as the overlap between wave functions n and j at sequential time steps.

Solving the time-dependent Schrodinger equation for the electrons with parametric dependence on nuclear coordinates is not sufficient for modeling electron−phonon relaxation dynamics. In particular, the nuclear trajectory, $\mathbf{R}(t)$, has to be specified. Most importantly, the electronic Schrodinger equation with parametric nuclear dependence cannot describe energy equilibration between electrons and nuclei and thus cannot achieve thermal equilibrium that exists in the long time-limit of electron−phonon relaxation.[59] In order to develop a proper description, one can modify the Schrodinger equation with nonlinear terms[60] or, most commonly, resort to a surface hopping (SH) technique.

SH is a stochastic algorithm for switching electronic states in a mixed quantum-classical simulation, which introduces correlations between the electronic and nuclear evolutions. SH can be viewed as a master equation with transition rates obtained by solving the time-dependent Schrodinger equation. FSSH[59] is the most popular SH algorithm, and it is suitable for the current study. The probability of a transition from state j to another state k within the time interval $\mathrm{d}t$ is given in FSSH by

$$\mathrm{d}P_{kj} = \frac{-2Re(\mathrm{d}_{jk}A_{jk}^*)}{A_{jj}}\mathrm{d}t;\ A_{jk} = C_jC_k^* \tag{5}$$

If the calculated $\mathrm{d}P_{kj}$ is negative, the probability is set as zero. The expression (5) minimizes the number of hops, hence the

DOI: 10.1021/acs.jpcc.9b06914
J. Phys. Chem. C 2019, 123, 22842−22850

"fewest switches" feature, because a hop is possible only when the occupation of the initial state j diminishes and the occupation of the final state k grows, and only when the two states are coupled via d_{jk}. In order to conserve the total electron−nuclear energy after a hop, the original FSSH introduces rescaling of nuclear velocities and hop rejection if there is not enough kinetic energy in the nuclear coordinate along the coupling direction $\langle\Phi_n|\nabla_R|\Phi_j\rangle$ to accommodate an increase in the electronic energy during the hop. The current implementation of FSSH[42] uses the classical path approximation (CPA), in which the velocity rescaling and hop rejection are replaced by multiplying the probability of transition, eq 5, upward in energy by the Boltzmann factor. The CPA is often applicable to condensed matter and nanoscale systems and leads to great computational savings, allowing us to perform *ab initio* NAMD simulations on systems composed of over 100 atoms and over 1000 electrons.

2.2. Simulation Details. All quantum-mechanical calculations and ab initio MD are performed with the Quantum Espresso (QE) simulation package,[61,62] which utilizes a plane-wave basis. The Perdew−Burke−Ernzerhof (PBE) generalized gradient functional[63] and the projector-augmented wave (PAW) approach[64] are used to describe interactions of ionic cores with valence electrons. The basis set cutoff energy is set to 60 Ry. Aiming to mimic the experimentally studied Au films with a narrow Ti adhesion layer,[38] and limited by simulation cell size, we construct an Au (111) surface with seven layers of Au atoms and a single layer of Ti atoms. Then, we substitute different numbers of Ti atoms into the first three layers of Au to simulate different alloy films. We also consider a pristine Au film. The alloy structures are chosen to represent different alloy characteristics, including alloy extent, i.e., the number of atoms intermixing between the two materials, alloying depth, i.e., the number of layers involved in the mixing, and atomic interactions, i.e., whether the extrinsic atoms are sufficiently close to interact chemically or are isolated. In order to be systematic, we attempt to vary one property at a time, e.g., keep the number of extrinsic atoms the same, while changing penetration depth, or consider the same penetration depth, while varying the number of extrinsic atoms. The optimized geometries of the six systems under investigation and the nomenclature are shown in Figure 1.

The simulation cell parameters are $a = b = 5.7676$ Å, $c = 41.1914$ Å, $\alpha = \beta = 90°$, and $\gamma = 120°$. The parameter c in the direction perpendicular to the surface includes 20 Å of vacuum in order to avoid spurious interactions between periodic images of the slabs. The $5 \times 5 \times 1$ Monkhorst−Pack k-point mesh is used for the structural optimization, and MD and NAMD simulations, and the $7 \times 7 \times 1$ mesh was employed for the DOS calculations.

After the structure optimization, repeated velocity rescaling is used to bring the temperature of the systems up to 300 K, corresponding to the temperatures in the experiment.[38] Following thermalization, 6 ps adiabatic MD trajectories are obtained for each system in the microcanonical ensemble with a 1 fs atomic time step, and are used for NAMD simulations. The NAC matrixes are calculated for each geometry along the MD trajectories, and FSSH simulations are performed by averaging over 2000 initial geometries and 2000 stochastic realizations of the FSSH process for each geometry.

Although more accurate DFT functionals are available, such functionals increase significantly the computational cost of the already computationally intense NAMD simulation. The most inexpensive correction to the PBE functional can be provided by a + U term. This term is often used for description of semiconductors, in which case it is tuned to reproduce the semiconductor bandgap. The current systems are metallic, and there is no clear experimental parameter to which the + U term can be fitted. Moreover, the + U value may depend on alloy stoichiometry. Therefore, we prefer not to introduce additional adjustable parameters in the calculation. A similar argument applies to hybrid functionals, which include an adjustable amount of the Hartree−Fock exchange. Further, Au is a heavy element, and spin−orbits (SO) interactions can play an important role. Unfortunately, introducing SO interaction into ab initio NAMD is not an easy task. The NAC calculation is more difficult with SO coupling, since wave functions become spinors, and the computational cost grows significantly. As will be seen below, the key conclusions of the current work are independent of alloy details, and we expect that they should also be robust changes to the DFT functional.

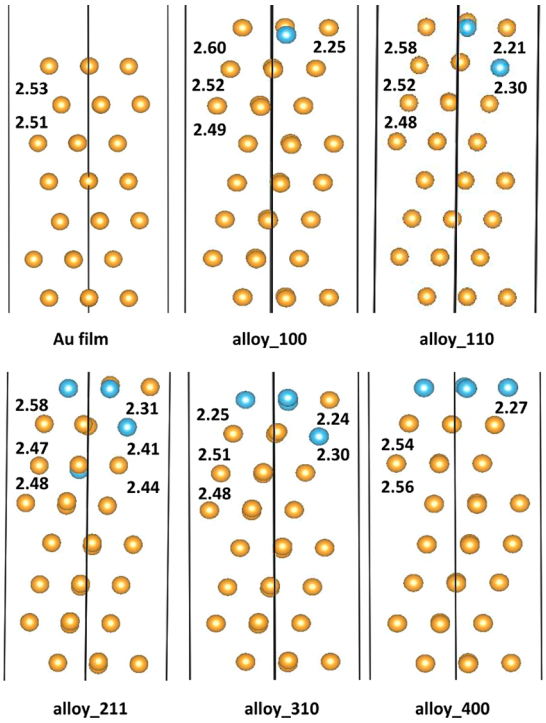

Figure 1. Side views of the optimized simulation cells for the Au (111) slab with a narrow Ti adhesion layer for different amount of alloying between Au and Ti. Ti atoms are blue and Au atoms are gold. The numbers on the left-hand-side show average vertical Au−Au distance between layers, and on the right-hand-side average vertical Au−Ti distances, in angstrom. The integers in alloy_klm refer to Ti atoms in the top three layers of the systems, respectively. For instance, alloy_400 describes a continuous monolayer of Ti, while alloy_310 has one of the four Ti atoms imbedded into the first layer of Au.

3. RESULTS AND DISCUSSION

We start by analyzing the geometric and electronic structure of the Au/Ti slabs. Such analyses are standard in all ab initio calculations. Then, we proceed to study electron-vibrational interactions using our state-of-the-art NAMD techniques[40] implemented within real-time TDDFT.[41−43] We report and discuss the NAC matrix elements, characterize the phonon modes that couple to the electronic subsystem, and analyze

DOI: 10.1021/acs.jpcc.9b06914
J. Phys. Chem. C 2019, 123, 22842−22850

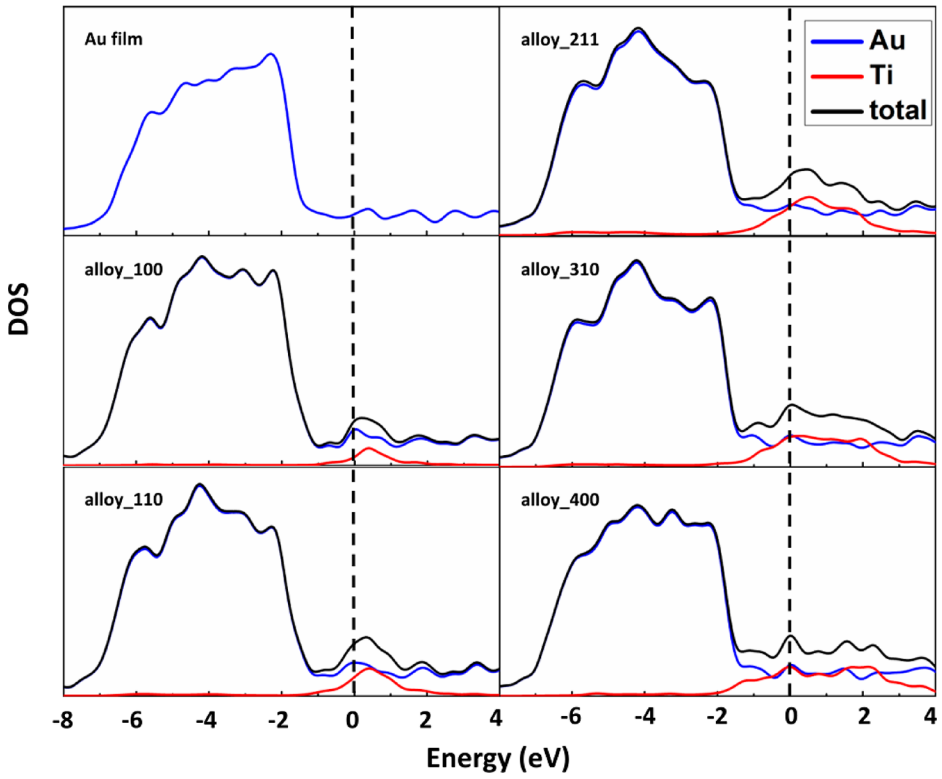

Figure 2. Total and partial densities of states (DOS) for the six systems in their optimized structures. The Fermi level is set to zero and shown by the dashed line. Isolated Ti atoms create states slightly above the Fermi energy of Au. As Ti−Ti bonds are formed, the Ti DOS broadens forming a wide band.

details of electron-vibrational energy exchange in the six different slabs under investigation.

3.1. Geometric and Electronic Structure. The optimized structures of the six systems are shown in Figure 1. The alloy simulations follow a naming convention where each digit in alloy_klm corresponds to the number of Ti atoms in a given layer of the Au. In other words, the first digit corresponds to the number of Ti on top of the Au slab, the second digit denotes the number of atoms in the first layer of the Au slab, and the third digit the number of Ti atoms in the third layer. The average vertical Au−Au distances between layers are presented in the left-hand-side of the cells, and the average vertical Au−Ti distances of Au−Ti are given on the right-hand-side. Compared to the pristine Au film, incorporation of Ti shrinks the distance between the Au layers slightly, while adhesion of a perfect Ti monolayer (alloy_400) increases the distance. Also, incorporation of Ti distorts planarity of Au layers. Thus, the Au−Au distance between the top layers in alloy_100 is 2.60 Å, while the Au−Ti distance is 2.25 Å. Similar distortions are seen in both layers of alloy_110. Two additional facts can be noticed with the more complex systems. First, as Ti enters the third layer (alloy_211), the distortion does not get worse but is alleviated. Second, the Au−Au and Au−Ti distances between the top two layers in alloy_310 are almost equivalent (2.25 and 2.24 Å), and are even shorter than for the perfect Ti adhesive (2.27 Å, alloy_400). Such layer distortions and contractions influence the shape of wave functions and affect the NAC values, eq 4. Generally, there are no clear trends in geometry distortions with Ti penetration depth.

Figure 2 shows electronic DOS in the six systems, split into contributions from Ti and Au. The data are obtained using the optimized geometries corresponding to 0 K. The Fermi level is set to zero. Since both Au and Ti are metals, none of the six systems have a bandgap. The electronic DOS is large and is completely dominated by Au in the energy range between −7 and −1 eV; Ti comes into play at energies above −1 eV, showing different patterns for different Ti concentrations and embedding depths. Generally, as Ti concentration increases, the magnitude of Ti partial DOS (PDOS) increases as well. For example, alloy_110 has a higher Ti PDOS than alloy_100, and alloy_211 has a higher Ti PDOS than alloy_110. When Ti concentration becomes sufficiently large so that Ti atoms start forming bonds approaching a continuous layer, Ti PDOS stops growing in magnitude and becomes broader. Considering systems with the same number of Ti atoms distributed differently between layers, i.e., alloy_211, alloy_310, and alloy_400, we observe different dependencies of Ti PDOS on energy. Thus, Ti PDOS in alloy_400 is roughly equal to Au PDOS around 0.5 eV, while it is slightly larger than Au PDOS in alloy_310 and significantly larger than Au PDOS in alloy_211. The trend is reversed at 2.0 eV. It is quite remarkable that Ti PDOS is as large as Au PDOS, since the alloys contain 7−31 times fewer Ti atoms than Au atoms. The large relative contribution of Ti PDOS to the total DOS at energies near the Fermi level and above constitute an important factor rationalizing the strong influence of thin Ti adhesion layers on electron−phonon energy exchange in Au films observed experimentally.[38]

Phonon-induced NAC between electronic states creates channels for hot electron relaxation. NAC values are related to the corresponding wave function overlap, according to eq 4. Therefore, we investigate the shape of electron densities at different energies. Considering the experimental[38] excitation

DOI: 10.1021/acs.jpcc.9b06914
J. Phys. Chem. C 2019, 123, 22842−22850

energy of 3.1 eV, we consider three energy ranges, 0−1, 1−2, and 2−3 eV, denoted by low, mid, and high. The 2−3 eV range includes states up to 3.1 eV. Figure 3 presents densities of electronic states averaged over these energy ranges, along with the HOMO charge density for each system.

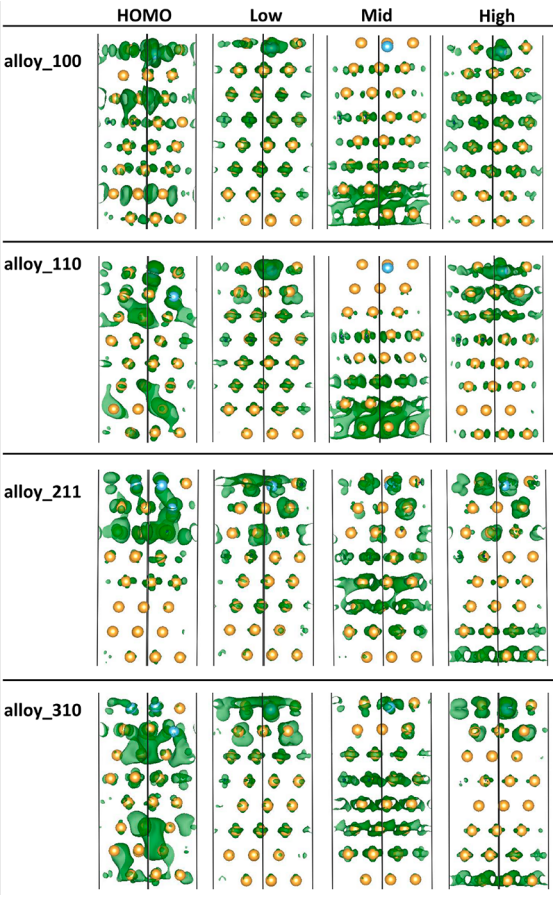

Figure 3. Charge density of HOMO and averaged charge densities of all states within different energy ranges. "low", "mid", and "high" correspond to 0−1, 1−2, and 2−3 eV above the Fermi energy.

The systems with lower Ti concentrations, alloy_100 and alloy_110, have similar charge density patterns. The charge densities are localized in the upper layers at high energies, in the lower layers at middle energies, and delocalized across the slabs at low energies. The systems with higher Ti concentrations, alloy_211 and alloy_310, also have similar charge density patterns. The charge densities are localized in the outer regions of the slabs at high energies, in the upper layers at low energies, and delocalized across the slabs at middle energies. The localization in the upper layers at low energies can be attributed to high Ti PDOS around 0.5 eV in alloy_211 and alloy_310.

The depth of the embedded Ti atoms also has interesting effect. For example, both HOMO and Low charge densities of alloy_100, alloy_110 and alloy_211 become more concentrated in the areas containing Ti atoms when the Ti atoms enter deeper into the second and third layers of the Au slab. At high energies, the densities are increasingly spread to the outer regions of the slab going from alloy_100 to alloy_110 to alloy_211.

Since both concentration and penetration depth of Ti atoms influence electronic wave functions, the electron−phonon relaxation time scales and mechanisms may be expected to differ among the systems. In order to quantify electron−phonon interactions, we perform a similar energy analysis of the NAC, Table 1.

3.2. Electron−Phonon Interactions. Table 1 compares the absolute NAC values averaged over all electronic state pairs within and between the low, mid, and high energy channels. The NAC values inside the channels (high, mid, and low) are larger than those between the channels (high-mid, high-low, and mid-low). This observation can be explained by the second part of eq 4 containing the energy difference in the denominator: The larger the energy gap, the smaller the NAC. This result implies that energy dissipation occurs primarily by transitions between nearby electronic states, and the instantaneous deposition of large amounts of electronic energy from these transitions into the phonons are rare.

Figure 4 shows energy relaxation curves of the six systems. The electrons are excited to 3.1 eV, as in the experiment,[38] and relax to the Fermi energy by coupling to phonons. The relaxation times obtained by exponential fitting are shown in the last column of Table 1. The energy relaxation times decrease in the sequence Au film > alloy_100 > alloy_400 > alloy_211 > alloy_110 > alloy_310. However, the times are similar in all systems except for the Au film and alloy_100. As long as Ti atoms are not isolated and are close enough to each other to interact chemically and form bonds, they create sufficiently wide bands in the DOS (Figure 2) and greatly accelerate the relaxation dynamics compared to pristine Au. On the other hand, if Ti atoms are not in immediate contact to form chemical bonds, Ti states do not form bands, and the contribution of Ti to the relaxation is much more limited. Figure 4 demonstrates that the large influence of a narrow Ti adhesion layer on electron−phonon relaxation in Au film

Table 1. Absolute NAC Averaged over States within Different Energy Ranges and between These Ranges in the Six Systems at 300 K[a]

	NAC (meV)								
	low	mid	high	high-mid	high-low	mid-low	0−3 eV	0−3 eV (RMS)	T (ps)
Au film	1.94	2.27	1.24	0.58	0.44	1.28	1.10	1.67	2.71
alloy_100	2.07	1.28	1.56	0.81	0.53	0.95	1.15	1.84	1.83
alloy_110	2.11	1.37	2.20	1.04	0.78	0.76	1.38	2.08	0.68
alloy_211	1.78	1.69	2.91	1.57	0.78	1.00	1.46	2.08	0.74
alloy_310	2.38	1.58	3.26	1.88	0.74	0.84	1.64	2.64	0.53
alloy_400	1.81	2.16	1.71	0.70	1.16	0.93	1.27	1.88	0.81

[a]"Low", "Mid", and "High" refer to 0−1, 1−2, and 2−3 eV above the Fermi energy. The last two column show root-mean-square (RMS) NAC and electron-phonon relaxation times.

DOI: 10.1021/acs.jpcc.9b06914
J. Phys. Chem. C 2019, 123, 22842−22850

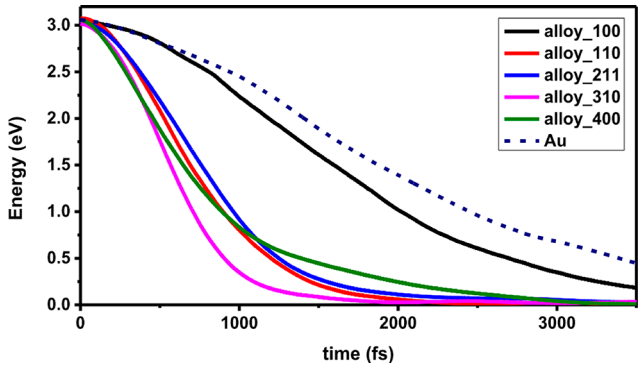

Figure 4. Electron−phonon energy relaxation in the six systems at 300 K. Ti accelerates the relaxation by introducing both high frequency phonons (see Figure 5) and additional electronic states within the relevant energy range (Figure 2). Except for the system with an isolated Ti atom, alloy_100, all other systems show similar relaxation times.

observed experimentally[38] is independent of details of the Au/Ti interfacial region. This is the main conclusion of the current work, indicating that the effect can be achieved in a robust manner.

The NAC value is the most important characteristic that determines the relaxation time. The differences in the electron−phonon relaxation times in the six systems can be rationalized by the differences in the absolute NAC averaged over the whole energy range (the 0−3 eV column in Table 1): The smaller the average absolute NAC value, the longer the relaxation time. At the same time, NAC fluctuates along a trajectory, and the absolute average values of NAC reported in Table 1 only provide a rough comparison of the NAC for the different systems. Additional information is reflected in the root-mean-square (RMS) values of the NAC, also reported in Table 1, column "0−3 eV RMS" in Table 1. The trends are similar between the two sets of the reported NAC measures; however, the RMS values are consistently larger than the absolute average values. This result indicates that NAC fluctuates rather significantly along the trajectory. This is because NAC exhibits a complex dependence on electronic wave functions and nuclear velocities, eq 4, both of which also fluctuate. The RMS NAC values can be more appropriate for a Fermi's golden rule type analysis,[65] since the Fermi's golden rule rate is proportional to coupling squared.

Note that previously we reported calculations[39] on the pristine Au film and the Au film covered with a Ti monolayer, alloy_400 in the current nomenclature, using the Pyxaid software with electronic structure input from VASP[66] rather than QE.[61,62] Currently, we repeated the calculations on these systems with QE and found that the NAC obtained with QE were smaller than those obtained previously with VASP. The origin of this difference can be attributed to eigensolvers that produce adiabatic wave functions, $\Phi_n(\mathbf{r};\mathbf{R}(t))$, eq 1. Namely, the phase/sign of adiabatic wave functions is not defined in an eigensolver and can change randomly along the trajectory. This phase/sign issue has to be treated properly, as shown by Akimov.[67] The current calculation treats the phase properly, while the previous publication[39] did not, since we were not aware of the problem. Importantly, all calculations discussed in the present work are performed using the same (corrected) methodology, and therefore, the results are consistent among the six systems under investigation.

The electron−phonon interactions can be characterized further by considering frequencies of the phonon modes that couple to the hot electrons. The frequencies can be obtained by computing Fourier transforms (FT) of energy gaps between electronic states. The data, known as spectral densities or influence spectra,[68−70] are shown in Figure 5. In particular, we

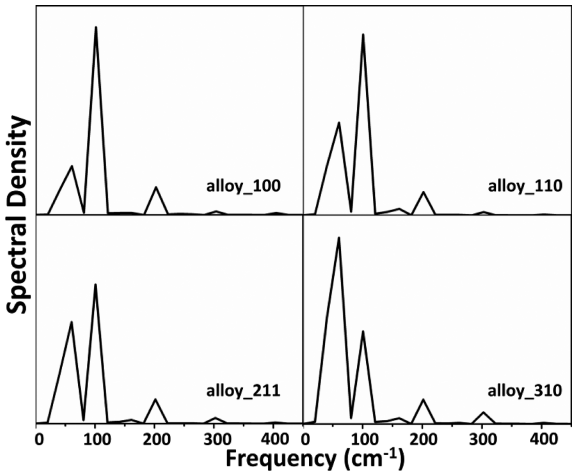

Figure 5. Averaged Fourier transforms of phonon-induced fluctuations of energy gaps between all pairs of states included into the NAMD simulation, from 0 to 3.1 eV above the Fermi energy. The higher peaks at lower energies arise from the heavier Au atoms, while the lower peaks at higher energies arise from the lighter Ti atoms.

compute and average the FTs of phonon-induced fluctuations of energy gaps between all pairs of states within the 0−3.1 eV energy window. The height of the signal at a particular frequency characterizes the strength of the coupling of the corresponding phonon to the relaxing electrons.

The spectral densities shown in Figure 5 are dominated by low frequency modes. The dominant peaks below 100 cm^{-1} can be assigned to phonon modes of Au atoms.[71] Ti atoms are four times lighter than Au atoms, and therefore, they introduce higher vibrational frequencies. The high frequency modes offer new electron−phonon relaxation channels. Since the NAC is proportional to nuclear velocity, eq 4, and nuclear velocity is higher for lighter atoms at a fixed temperature, which determines kinetic energy, lighter Ti introduce faster motions and increase the NAC. Interestingly, the intensities of the higher frequency peaks rise only slightly with increasing concentration of Ti atoms, compare top and bottom panels in Figure 5 and are generally independent of the alloy details. This result further confirms the main conclusion of the work, that atomistic details of the Au/Ti interfacial region have little influence on the electron−phonon relaxation, confirming robustness of the experimental results.[38]

4. CONCLUSIONS

In summary, we have simulated the hot electron relaxation process in six Au/Ti systems representing experimentally studied Au slabs with thin Ti adhesion layers. The systems contain different alloying patterns at the Au/Ti interface. The experiments show that a thin Ti layer greatly accelerates electron−phonon energy transfer, and our calculations rationalize this observation. The calculations also show that the acceleration is independent of the atomistic details of the Au/Ti interface, as long as Ti atoms imbedded into Au are not

DOI: 10.1021/acs.jpcc.9b06914
J. Phys. Chem. C 2019, 123, 22842−22850

isolated. The electron−phonon relaxation is accelerated because Ti has a much smaller atomic mass than Au, introducing high frequency lattice vibrations, and because Ti exhibits high DOS within the relevant energy range near the Fermi energy of Au. Even isolated Ti atoms introduce high frequency vibrations; however, they create a very local DOS that does not cover all relevant energies. If Ti atoms are capable to interact, either in clusters or a continuous film, the energy range of the Ti DOS broadens, and the electron−phonon relaxation is significantly accelerated. The electron−phonon relaxation proceeds by multiple rapid transitions exchanging small amounts of energy, rather than by rare events exchanging large energy quanta, in particular, because nonadiabatic electron−phonon coupling decreases as the energy difference between electronic states increases. The robust acceleration of the electron−phonon energy flow in Au slabs by Ti adhesion layers is beneficial for the development of nanoscale devices requiring efficient energy exchange, for example, to achieve heat dissipation. The lessons learned from the reported simulations suggest that efficient heat transfer can be achieved in nanoscale systems by utilizing low concentrations of light atoms that have electronic states within the desired energy range. A judicious application of such strategy can be used, for instance, to achieve different rates of relaxations of electrons vs holes, and to design materials in which the relaxation rate depends on carrier energy to accumulate multiple hot charges at energies needed for efficient photo- and electro-catalysis. The general principles established in this study can be used to control and manipulate highly nonequilibrium electron−phonon distributions on ultrafast time scales.

AUTHOR INFORMATION

Corresponding Author

*E-mail: prezhdo@usc.edu.

ORCID

Xin Zhou: 0000-0002-4385-8379

Patrick E. Hopkins: 0000-0002-3403-743X

Oleg V. Prezhdo: 0000-0002-5140-7500

Notes

The authors declare no competing financial interest.

ACKNOWLEDGMENTS

Financial support from the U.S. Department of Defense, Multidisciplinary University Research Initiative, Grant No. W911NF-16-1-0406 is gratefully acknowledged.

REFERENCES

(1) Lynn, J. W.; Smith, H. G.; Nicklow, R. M. Lattice Dynamics of Gold. *Phys. Rev. B* **1973**, *8*, 3493−3499.

(2) Encina, E. R.; Coronado, E. A. Resonance Conditions for Multipole Plasmon Excitations in Noble Metal Nanorods. *J. Phys. Chem. C* **2007**, *111*, 16796−16801.

(3) Lin, Z.; Zhigilei, L. V.; Celli, V. Electron-Phonon Coupling and Electron Heat Capacity of Metals under Conditions of Strong Electron-Phonon Nonequilibrium. *Phys. Rev. B: Condens. Matter Mater. Phys.* **2008**, *77*, 075133.

(4) Demartini, A.; Alloisio, M.; Cuniberti, C.; Dellepiane, G.; Jadhav, S. A.; Thea, S.; Giorgetti, E.; Gellini, C.; Muniz-Miranda, M. Polydiacetylene-Functionalized Noble Metal Nanocages. *J. Phys. Chem. C* **2009**, *113*, 19475−19481.

(5) Yokota, K.; Taniguchi, M.; Kawai, T. Metal−Molecule Interfaces Formed by Noble-Metal−Chalcogen Bonds for Nanoscale Molecular Devices. *J. Phys. Chem. C* **2010**, *114*, 4044−4050.

(6) Kooij, E. S.; Ahmed, W.; Zandvliet, H. J. W.; Poelsema, B. Localized Plasmons in Noble Metal Nanospheroids. *J. Phys. Chem. C* **2011**, *115*, 10321−10332.

(7) Sai, V. V. R.; Gangadean, D.; Niraula, I.; Jabal, J. M. F.; Corti, G.; McIlroy, D. N.; Eric Aston, D.; Branen, J. R.; Hrdlicka, P. J. Silica Nanosprings Coated with Noble Metal Nanoparticles: Highly Active Sers Substrates. *J. Phys. Chem. C* **2011**, *115*, 453−459.

(8) Zhou, Y.; Fichthorn, K. A. Internal Stress-Induced Orthorhombic Phase in 5-Fold-Twinned Noble Metal Nanowires. *J. Phys. Chem. C* **2014**, *118*, 18746−18755.

(9) Giri, A.; Hopkins, P. E. Transient Thermal and Nonthermal Electron and Phonon Relaxation after Short-Pulsed Laser Heating of Metals. *J. Appl. Phys.* **2015**, *118*, 215101.

(10) Ma, W.; Miao, T.; Zhang, X.; Kohno, M.; Takata, Y. Comprehensive Study of Thermal Transport and Coherent Acoustic-Phonon Wave Propagation in Thin Metal Film−Substrate by Applying Picosecond Laser Pump−Probe Method. *J. Phys. Chem. C* **2015**, *119*, 5152−5159.

(11) Hao, J.; Liu, T.; Huang, Y.; Chen, G.; Liu, A.; Wang, S.; Wen, W. Metal Nanoparticle−Nanowire Assisted Sers on Film. *J. Phys. Chem. C* **2015**, *119*, 19376−19381.

(12) Liu, T.; Hao, J.; Wan, F.; Huang, Y.; Su, X.; Hu, L.; Chen, W.; Fang, Y. Heterodimer Nanostructures Induced Energy Focusing on Metal Film. *J. Phys. Chem. C* **2016**, *120*, 7778−7784.

(13) Encina, E. R.; Coronado, E. A. Size Optimization of Iron Oxide@Noble Metal Core−Shell Nanohybrids for Photothermal Applications. *J. Phys. Chem. C* **2016**, *120*, 5630−5639.

(14) Trew, R. J. Sic and Gan Transistors-Is There One Winner for Microwave Power Applications? *Proc. IEEE* **2002**, *90*, 1032−1047.

(15) Robertson, J. High Dielectric Constant Gate Oxides for Metal Oxide Si Transistors. *Rep. Prog. Phys.* **2006**, *69*, 327−396.

(16) Rowlette, J. A.; Goodson, K. E. Fully Coupled Nonequilibrium Electron−Phonon Transport in Nanometer-Scale Silicon Fets. *IEEE Trans. Electron Devices* **2008**, *55*, 220−232.

(17) Pop, E. Energy Dissipation and Transport in Nanoscale Devices. *Nano Res.* **2010**, *3*, 147−169.

(18) Banlusan, K.; Strachan, A. Shockwave Energy Dissipation in Metal−Organic Framework Mof-5. *J. Phys. Chem. C* **2016**, *120*, 12463−12471.

(19) Lu, Z.; Wang, Y.; Ruan, X. Metal/Dielectric Thermal Interfacial Transport Considering Cross-Interface Electron-Phonon Coupling: Theory, Two-Temperature Molecular Dynamics, and Thermal Circuit. *Phys. Rev. B: Condens. Matter Mater. Phys.* **2016**, *93*, 064302.

(20) Li, G.; Movaghar, B.; Ratner, M. A. Electron−Phonon Coupling Effect on Charge Transfer in Nanostructures. *J. Phys. Chem. C* **2013**, *117*, 850−857.

(21) Mueller, B. Y.; Rethfeld, B. Relaxation Dynamics in Laser-Excited Metals under Nonequilibrium Conditions. *Phys. Rev. B: Condens. Matter Mater. Phys.* **2013**, *87*, 035139.

(22) Dacosta Fernandes, B.; Le Beulze, A.; Moroté, F.; Oberlé, J.; Tréguer-Delapierre, M.; Burgin, J.; Langot, P. Electron−Phonon Scattering in 2d Silver Nanotriangles. *J. Phys. Chem. C* **2013**, *117*, 22041−22045.

(23) Gaur, A. P. S.; Sahoo, S.; Scott, J. F.; Katiyar, R. S. Electron−Phonon Interaction and Double-Resonance Raman Studies in Monolayer Ws2. *J. Phys. Chem. C* **2015**, *119*, 5146−5151.

(24) Zhou, Z.; Liu, J.; Long, R.; Li, L.; Guo, L.; Prezhdo, O. V. Control of Charge Carriers Trapping and Relaxation in Hematite by Oxygen Vacancy Charge: Ab Initio Non-Adiabatic Molecular Dynamics. *J. Am. Chem. Soc.* **2017**, *139*, 6707−6717.

(25) Zhou, X.; Li, L.; Dong, H.; Giri, A.; Hopkins, P. E.; Prezhdo, O. V. Temperature Dependence of Electron−Phonon Interactions in Gold Films Rationalized by Time-Domain Ab Initio Analysis. *J. Phys. Chem. C* **2017**, *121*, 17488−17497.

DOI: 10.1021/acs.jpcc.9b06914
J. Phys. Chem. C 2019, 123, 22842−22850

(26) Elsayed-Ali, H. E.; Norris, T. B.; Pessot, M. A.; Mourou, G. A. Time-Resolved Observation of Electron-Phonon Relaxation in Copper. *Phys. Rev. Lett.* **1987**, *58*, 1212−1215.
(27) Mueller, B. Y.; Rethfeld, B. Nonequilibrium Electron−Phonon Coupling after Ultrashort Laser Excitation of Gold. *Appl. Surf. Sci.* **2014**, *302*, 24−28.
(28) Grumstrup, E. M.; Gabriel, M. M.; Cating, E. M.; Pinion, C. W.; Christesen, J. D.; Kirschbrown, J. R.; Vallorz, E. L.; Cahoon, J. F.; Papanikolas, J. M. Ultrafast Carrier Dynamics in Individual Silicon Nanowires: Characterization of Diameter-Dependent Carrier Lifetime and Surface Recombination with Pump−Probe Microscopy. *J. Phys. Chem. C* **2014**, *118*, 8634−8640.
(29) Walsh, B. R.; Sonnichsen, C.; Mack, T. G.; Saari, J. I.; Krause, M. M.; Nick, R.; Coe-Sullivan, S.; Kambhampati, P. Excited State Phononic Processes in Semiconductor Nanocrystals Revealed by Excitonic State-Resolved Pump/Probe Spectroscopy. *J. Phys. Chem. C* **2019**, *123*, 3868−3875.
(30) Anisimov, S.; Kapeliovich, B.; Perelman, T. J. Z. E. T. F. Electron Emission from Metal Surfaces Exposed to Ultrashort. *Laser Pulses* **1974**, *66*, 375−377.
(31) Qiu, T.; Tien, C. J. J. o. H. T. Heat Transfer Mechanisms During Short-Pulse. *J. Heat Transfer* **1993**, *115*, 835−841.
(32) Yu, P.; Tang, J.; Lin, S.-H. Photoinduced Structural Dynamics in Laser-Heated Nanomaterials of Various Shapes and Sizes. *J. Phys. Chem. C* **2008**, *112*, 17133−17137.
(33) Strasser, M.; Setoura, K.; Langbein, U.; Hashimoto, S. Computational Modeling of Pulsed Laser-Induced Heating and Evaporation of Gold Nanoparticles. *J. Phys. Chem. C* **2014**, *118*, 25748−25755.
(34) Avanesian, T.; Christopher, P. Adsorbate Specificity in Hot Electron Driven Photochemistry on Catalytic Metal Surfaces. *J. Phys. Chem. C* **2014**, *118*, 28017−28031.
(35) Eesley, G. L. Generation of Nonequilibrium Electron and Lattice Temperatures in Copper by Picosecond Laser Pulses. *Phys. Rev. B: Condens. Matter Mater. Phys.* **1986**, *33*, 2144−2151.
(36) Chen, J. K.; Latham, W. P.; Beraun, J. E. The Role of Electron−Phonon Coupling in Ultrafast Laser Heating. *J. Laser Appl.* **2005**, *17*, 63−68.
(37) Majumdar, A.; Reddy, P. Role of Electron−Phonon Coupling in Thermal Conductance of Metal−Nonmetal Interfaces. *Appl. Phys. Lett.* **2004**, *84*, 4768−4770.
(38) Giri, A.; Gaskins, J. T.; Donovan, B. F.; Szwejkowski, C.; Warzoha, R. J.; Rodriguez, M. A.; Ihlefeld, J.; Hopkins, P. E. Mechanisms of Nonequilibrium Electron-Phonon Coupling and Thermal Conductance at Interfaces. *J. Appl. Phys.* **2015**, *117*, 105105.
(39) Zhou, X.; Jankowska, J.; Li, L.; Giri, A.; Hopkins, P. E.; Prezhdo, O. V. Strong Influence of Ti Adhesion Layer on Electron-Phonon Relaxation in Thin Gold Films: Ab Initio Nonadiabatic Molecular Dynamics. *ACS Appl. Mater. Interfaces* **2017**, *9*, 43343−43351.
(40) Wang, L. J.; Akimov, A.; Prezhdo, O. V. Recent Progress in Surface Hopping: 2011−2015. *J. Phys. Chem. Lett.* **2016**, *7*, 2100−2112.
(41) Craig, C. F.; Duncan, W. R.; Prezhdo, O. V. Trajectory Surface Hopping in the Time-Dependent Kohn-Sham Approach for Electron-Nuclear Dynamics. *Phys. Rev. Lett.* **2005**, *95*, 163001.
(42) Akimov, A. V.; Prezhdo, O. V. The Pyxaid Program for Non-Adiabatic Molecular Dynamics in Condensed Matter Systems. *J. Chem. Theory Comput.* **2013**, *9*, 4959−4972.
(43) Akimov, A. V.; Prezhdo, O. V. Advanced Capabilities of the Pyxaid Program: Integration Schemes, Decoherence Effects, Multi-excitonic States, and Field-Matter Interaction. *J. Chem. Theory Comput.* **2014**, *10*, 789−804.
(44) Tully, J. C. Molecular Dynamics with Electronic Transitions. *J. Chem. Phys.* **1990**, *93*, 1061−1071.
(45) Neukirch, A. J.; Guo, Z.; Prezhdo, O. V. Time-Domain Ab Initio Study of Phonon-Induced Relaxation of Plasmon Excitations in a Silver Quantum Dot. *J. Phys. Chem. C* **2012**, *116*, 15034−15040.
(46) Akimov, A. V.; Prezhdo, O. V. Nonadiabatic Dynamics of Charge Transfer and Singlet Fission at the Pentacene/C60 Interface. *J. Am. Chem. Soc.* **2014**, *136*, 1599−1608.
(47) Jankowska, J.; Prezhdo, O. V. Ferroelectric Alignment of Organic Cations Inhibits Nonradiative Electron-Hole Recombination in Hybrid Perovskites: Ab Initio Nonadiabatic Molecular Dynamics. *J. Phys. Chem. Lett.* **2017**, *8*, 812−818.
(48) Long, R.; Fang, W.-H.; Prezhdo, O. V. Strong Interaction at the Perovskite/Tio2 Interface Facilitates Ultrafast Photoinduced Charge Separation: A Nonadiabatic Molecular Dynamics Study. *J. Phys. Chem. C* **2017**, *121*, 3797−3806.
(49) Long, R.; Prezhdo, O. V.; Fang, W. Nonadiabatic Charge Dynamics in Novel Solar Cell Materials. *Wiley Interdisciplinary Reviews-Computational Molecular Science* **2017**, *7*, No. e1305.
(50) Nam, Y.; Li, L.; Lee, J. Y.; Prezhdo, O. V. Size and Shape Effects on Charge Recombination Dynamics of Tio2 Nanoclusters. *J. Phys. Chem. C* **2018**, *122*, 5201−5208.
(51) He, J. L.; Fang, W. H.; Long, R.; Prezhdo, O. V. Superoxide/Peroxide Chemistry Extends Charge Carriers' Lifetime but Undermines Chemical Stability of Ch3nh3pbi3 Exposed to Oxygen: Time-Domain Ab Initio Analysis. *J. Am. Chem. Soc.* **2019**, *141*, 5798−5807.
(52) Zhang, L. L.; Vasenko, A. S.; Zhao, J.; Prezhdo, O. V. Mono-Elemental Properties of 2d Black Phosphorus Ensure Extended Charge Carrier Lifetimes under Oxidation: Time-Domain Ab Initio Analysis. *J. Phys. Chem. Lett.* **2019**, *10*, 1083−1091.
(53) Li, L. Q.; Long, R.; Prezhdo, O. V. Why Chemical Vapor Deposition Grown Mos2 Samples Outperform Physical Vapor Deposition Samples: Time-Domain Ab Initio Analysis. *Nano Lett.* **2018**, *18*, 4008−4014.
(54) Hyeon-Deuk, K.; Prezhdo, O. V. Multiple Exciton Generation and Recombination Dynamics in Small Si and Cdse Quantum Dots: An Ab Initio Time-Domain Study. *ACS Nano* **2012**, *6*, 1239−1250.
(55) Wang, L. J.; Long, R.; Prezhdo, O. V. Time-Domain Ab Initio Modeling of Photoinduced Dynamics at Nanoscale Interfaces. *Annu. Rev. Phys. Chem.* **2015**, *66*, 549−579.
(56) Chaban, V. V.; Prezhdo, V. V.; Prezhdo, O. V. Covalent Linking Greatly Enhances Photoinduced Electron Transfer in Fullerene-Quantum Dot Nanocomposites: Time-Domain Ab Initio Study. *J. Phys. Chem. Lett.* **2013**, *4*, 1−6.
(57) Fischer, S. A.; Duncan, W. R.; Prezhdo, O. V. Ab Initio Nonadiabatic Molecular Dynamics of Wet-Electrons on the Tio2 Surface. *J. Am. Chem. Soc.* **2009**, *131*, 15483−15491.
(58) Zhou, X.; Tokina, M. V.; Tomko, J. A.; Braun, J. L.; Hopkins, P. E.; Prezhdo, O. V. Thin Ti Adhesion Layer Breaks Bottleneck to Hot Hole Relaxation in Au Films. *J. Chem. Phys.* **2019**, *150*, 184701.
(59) Parandekar, P. V.; Tully, J. C. Mixed Quantum-Classical Equilibrium. *J. Chem. Phys.* **2005**, *122*, 094102.
(60) Nijjar, P.; Jankowska, J.; Prezhdo, O. V. Ehrenfest and Classical Path Dynamics with Decoherence and Detailed Balance. *J. Chem. Phys.* **2019**, *150*, 204124.
(61) Giannozzi, P.; Baroni, S.; Bonini, N.; Calandra, M.; Car, R.; Cavazzoni, C.; Ceresoli, D.; Chiarotti, G. L.; Cococcioni, M.; Dabo, I.; et al. Quantum Espresso: A Modular and Open-Source Software Project for Quantum Simulations of Materials. *J. Phys.: Condens. Matter* **2009**, *21*, 395502.
(62) Giannozzi, P.; Andreussi, O.; Brumme, T.; Bunau, O.; Nardelli, M. B.; Calandra, M.; Car, R.; Cavazzoni, C.; Ceresoli, D.; Cococcioni, M.; et al. Advanced Capabilities for Materials Modelling with Quantum Espresso. *J. Phys.: Condens. Matter* **2017**, *29*, 465901.
(63) Perdew, J. P.; Burke, K.; Ernzerhof, M. Generalized Gradient Approximation Made Simple. *Phys. Rev. Lett.* **1996**, *77*, 3865. Perdew, J. P. *Phys. Rev. Lett.* **1997**, *78*, 1396−1396.
(64) Blochl, P. E. Projector Augmented-Wave Method. *Phys. Rev. B: Condens. Matter Mater. Phys.* **1994**, *50*, 17953−17979.
(65) Hyeon-Deuk, K.; Madrid, A. B.; Prezhdo, O. V. Symmetric Band Structures and Asymmetric Ultrafast Electron and Hole Relaxations in Silicon and Germanium Quantum Dots: Time-Domain Ab Initio Simulation. *Dalton Transactions* **2009**, 10069−10077.

DOI: 10.1021/acs.jpcc.9b06914
J. Phys. Chem. C 2019, 123, 22842−22850

(66) Kresse, G.; Furthmüller, J. Efficient Iterative Schemes for Ab Initio Total-Energy Calculations Using a Plane-Wave Basis Set. *Phys. Rev. B: Condens. Matter Mater. Phys.* **1996**, *54*, 11169−11186.
(67) Akimov, A. V. A Simple Phase Correction Makes a Big Difference in Nonadiabatic Molecular Dynamics. *J. Phys. Chem. Lett.* **2018**, *9*, 6096−6102.
(68) Kamisaka, H.; Kilina, S. V.; Yamashita, K.; Prezhdo, O. V. Ab Initio Study of Temperature- and Pressure Dependence of Energy and Phonon-Induced Dephasing of Electronic Excitations in Cdse and Pbse Quantum Dots. *J. Phys. Chem. C* **2008**, *112*, 7800−7808.
(69) Pal, S.; Nijjar, P.; Frauenheim, T.; Prezhdo, O. V. Atomistic Analysis of Room Temperature Quantum Coherence in Two-Dimensional Cdse Nanostructures. *Nano Lett.* **2017**, *17*, 2389−2396.
(70) Akimov, A. V.; Prezhdo, O. V. Persistent Electronic Coherence Despite Rapid Loss of Electron-Nuclear Correlation. *J. Phys. Chem. Lett.* **2013**, *4*, 3857−3864.
(71) Miller, S. A.; Womick, J. M.; Parker, J. F.; Murray, R. W.; Moran, A. M. Femtosecond Relaxation Dynamics of Au25l18− Monolayer-Protected Clusters. *J. Phys. Chem. C* **2009**, *113*, 9440−9444.

DOI: 10.1021/acs.jpcc.9b06914
J. Phys. Chem. C 2019, 123, 22842−22850